Methods for Partial Discharge Calibration in Gas-Insulated Substations for HVDC Power Grids and Charge Evaluation Uncertainty

Mier, Christian; Khamlichi, Abderrahim; Dalstein, Matthieu; Vidal, Jose Ramon; Garnacho, Fernando; Mor, Armando Rodrigo; Vu-Cong, Thanh

DOI
10.1109/JSEN.2023.3302871

Publication date
2023

Document Version
Accepted author manuscript

Published in
IEEE Sensors Journal

Methods for Partial Discharge Calibration in Gas-Insulated Substations for HVDC Power Grids and Charge Evaluation Uncertainty

Christian Mier, Abderrahim Khamlichi, Matthieu Dalstein, José Ramón Vidal, Fernando Garnacho, Armando Rodrigo Mor and Thanh Vu-Cong.

***Abstract*—Driven by the voltage increase in high-voltage direct current (HVDC) Gas-insulated substations (GIS), novel methods are needed for partial discharge (PD) detection and monitoring. This paper shows a PD calibration method for very-high frequency magnetic and electric sensors in GIS. The calibration method uncertainty is tested in three laboratories using a low-voltage (LV) test bench and a high-voltage (HV) full-scale GIS. In the LV test, the calibration method's linearity, signal-to-noise ratio, and pulse width were compared against a reference charge, resulting in an error of around ±10%. The HV test consisted of different artificial defects introduced in a full-scale GIS, resulting in errors of around ±30%. The uncertainty is attributed mainly to random noise, which is critical in the charge estimation method. The electric and magnetic sensor combination showed better results, especially in the full-scale GIS, where reflections play an important role. This research has been performed in the framework of the project Future Energy 19ENG02 of EURAMET, resulting in a calibration method with the potential to measure PD pulses and discriminate impulse interferences, giving an advantage over conventional and ultra-high frequency methods.**

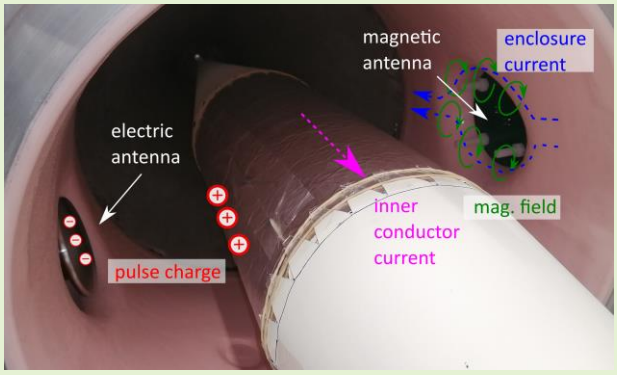

***Index Terms*— calibration, GIS, partial discharges, uncertainty**

I. Introduction

THE interest in a more sustainable power grid has increased the demand for high-voltage direct current (HVDC) gas-insulated substations (GIS) with remote electric insulation monitoring. Partial discharges (PD) measurements are an accepted tool for electric insulation diagnosis and are part of the GIS requirement in the standard IEC 62271 [1], which refers to the conventional PD test covered in the IEC 60270 [2]. The conventional method assumes that the measured PD apparent charge is proportional to the calibration charge, which is not true for electrically large equipment such as cables, gas-insulated lines, and GIS. Additionally, the connection of a coupling capacitor complicates remote monitoring. For that reason, IEC 62478 [3] recommends unconventional PD measuring methods, including ultra-high frequency (UHF) and very-high frequency (VHF) electromagnetic methods. The UHF is the most popular method due to its high noise rejection; however, the PD wave shape and charge information is lost in the frequency above the transverse electromagnetic mode. The PD wave shape and charge magnitude are important diagnosis parameters to classify the defect [4], evaluate its severity, and normalize measurements from different sensors [5].

The VHF sensors cover solely the transverse electromagnetic mode in GIS, enabling the extraction of the PD charge information and wave shape [5]. Reference [6] shows that VHF magnetic and electric sensors installed in the GIS mounting holes can be calibrated to estimate the PD charge. The electric sensor couples the propagated PD electric field, and the magnetic sensor couples the magnetic field produced by the PD current around the mounting hole, as shown in the abstract figure. Both sensors have a derivative response represented in (1), where V_o is the sensor's output, I_{pd} is the PD current, k is the calibration constant, ω_1 is the first pole, and ω_2 is the second pole. The magnetic antenna's calibration constant, k_m, is the coupling inductance M. For the

This project 19ENG02 FutureEnergy has received funding from the EMPIR programme co-financed by the Participating States and from the European Union's Horizon 2020 research and innovation programme. Funder ID: 10.13039/100014132.

C. Mier is with the department High Voltage Technologies at Delft University of Technology, Delft, 2628 CN Netherlands (e-mail: c.mierescurra@tudelft.nl).

A. Khamlichi, J. R. Vidal and F. Garnacho are with Laboratorio Central Oficial de Electrotencia, Madrid, 28906 Spain (e-mails: ak@ffii.es, jose.vidal@ffii.es, fernando.garnacho@ffii.es)

M. Dalstein and T. Vu-Cong are with Super Grid Institute, Villeurbanne, 69100 France (e-mail: Matthieu.DALSTEIN@supergrid-institute.com, thanh.vu@rte-france.com).

A. Rodrigo Mor is with Universitat Politècnica de València, Instituto de Tecnología Eléctrica, Valencia, 46022 Spain (e-mail: arrodmor@ite.upv.es).

electric antenna, k_e is the product of the coupling capacitor (C_1), the sensor's load (R), and the GIS characteristic impedance Z_0 ($k_e = C_1 \cdot R \cdot Z_0$). The magnetic sensor's ω_1 is the load and self-inductance (L_s) quotient, and for the electric sensor is the inverse product of the ground capacitance (C_2) and the load.

$$\frac{V_o(s)}{I_{pd}(s)} = H(s) \approx \frac{sk}{s^2\omega_2^{\,2} + s\omega_1 + 1} \tag{1}$$

The derivative response of electric and magnetic sensors enables the charge calculation using the voltage-double-integral method (V2I) [7]. This method proposes that the charge, Q, is proportional to the sensor's output voltage double integration and inversely proportional to the calibration constant (2). Due to high noise in on-site GIS, the integration must be limited to the pulse second zero crossing (t_0), giving some error in the estimated charge. This calibration constant can be found in the frequency domain and is equal to the sensors' transfer function slope in the low-frequency range (3). The noise and the integration time limit (t_0) increase the charge estimation error. Pulse overlapping is another uncertainty source, which can be reduced by combining both sensors.

$$Q \approx \frac{1}{k}\int_0^{t_0}\int_0^{t_0} V_o(t)\,dtdt \tag{2}$$

$$k \approx lim\left|\frac{H(\omega)}{\omega}\right|_{\omega\to 0} \quad when\ \omega \neq 0 \tag{3}$$

Reference [8] proposes the "synergy " method to improve the charge estimation and wave shape construction by combining the electric and magnetic antennas. An incident PD voltage (V^+) is linked with the PD current (I^+) by the characteristic impedance (Z_0). When there is a discontinuity in the pulse propagation, backward reflected waves result in voltage (V^-) and current (I^-) with opposite polarity, as shown in (4). This phenomenon can be used to detect the PD power flow and discern forward and backward components. The sensors can be normalized by scaling one of the sensor's outputs and adding them up to find the forward components (5), where α is the scaling factor, and the subscript "1" refers to one sensor and "2" to the other. Therefore, the overlapped pulses can be corrected to reduce the charge estimation uncertainty.

$$I^+(z,t) = \frac{V^+(z,t)}{Z_0} \ and\ I^-(z,t) = -\frac{V^-(z,t)}{Z_0} \tag{4}$$

$$V_1(t) + \alpha(t)V_2(t) = 2V_1^+(t) \tag{5}$$

The measurement error quantifies the uncertainty of a measuring system. This error is composed of a random component and a systematic component. Random errors arise from stochastic variations on influence quantities, and systematic error comes from a recognized effect of an influence quantity. The random error can be corrected by averaging an infinite number of measurements of the same measurand carried out under repeatability conditions ([9] and [10]). White noise is critical in the calibration method, and PD measurements cannot be averaged since every sample is different, and the condition is not repeatable. The influence of these errors in the measuring system is evaluated with uncertainty.

This paper evaluates a new calibration method for PD in GIS. The uncertainty is estimated in a low-voltage (LV) test bench free of reflections and in a full-scale GIS. The measuring system repeatability was tested in 3 laboratories: Delft University of Technology (TUDelft) in Delft, Netherlands; Laboratorio Central Oficial de Electrotecnia (LCOE) in Madrid, Spain; and SuperGrid Institute (SGI) in Lyon, France. The sensors' linearity, pulse width, and noise were evaluated in the LV test bench for the first two laboratories. In the full-scale GIS, real PD with different defects were considered. This paper first explains each laboratory's test setups and sensors. Then the methods used to calibrate and characterize the sensors are presented. And in the last section, the results are shown and discussed. This paper analyses the uncertainty and interoperability of the VHF calibration method for PD sensors in three scenarios.

II. VHF SENSOR'S CALIBRATION FOR PD CHARGE ESTIMATION

The first part explains the test setups used for the calibration procedure and the uncertainty analysis. Then, the sensors are described, characterized, and calibrated in the second part.

A. Test setups and calibration methodology

The calibration method uncertainty was assessed with a calibrated reference in a LV test setup. Furthermore, a full-scale GIS with real PD was used to evaluate the measuring system in a real situation.

The LV tests were conducted in test benches using calibrated PD pulses as a reference. TUDelft and LCOE used a full-scale GIS section adapted to impedance-matching cones to reduce reflections [11]. From this LV characterization, calibration constants for the VHF sensors were obtained. PD charge linearity, pulse width, and noise level tests were analyzed, considering that these factors depend not only on the sensor but also on the signal processing (software) and the signal conditioning (hardware). The measurements were carried out with calibrated oscilloscopes. The uncertainty of these oscilloscopes is negligible compared to the evaluated measuring system.

Once the sensors' characterization was performed, high-voltage (HV) tests were carried out in the three laboratories using representative defects in GIS. Each laboratory used different HV voltage sources, PD defects, and reference sensors.

1) *Low-voltage test setup*

TUDelft and LCOE participated with the LV test benches, explained as follows.

TUDelft used the test bench presented in Fig. 1. The calibration process was performed with a vector network analyzer connected to the input port and the sensor's outputs. For the uncertainty tests, the calibrator and the noise were

injected at the input port and measured with an oscilloscope at the output cone. The electric and magnetic antennas were mounted and connected to the oscilloscope through Mini-Circuits ZFL-500LN+ amplifiers. The linearity test was performed with an "LDC-5/UHF" calibrator injecting 5 pC (minimum allowed charge according to [12]) to 500 pC. The noise test was performed with the same calibrator injecting a constant 26 pC pulse in parallel with a 200 MHz white noise from 100 mV up to 1 V. Reference [13] demonstrates that an SF_6 PD has a duration below 1 ns, which is not the case for new alternative gases, having slower pulses [14]. Therefore, pulses from 11 to 400 ns were injected using a wave generator.

Fig. 1 TUDelft LV test bench.

LCOE used the test bench shown in Fig. 2. It consists of a 7 m-long full-scale GIS with a 50 Ω characteristic impedance. At 1.8 m from the injection point, the antennas were installed and connected directly to the high-bandwidth digital oscilloscope (without amplifiers). Then, the GIS was terminated with a 30 kV, 20 m long cable. The linearity test was carried out with an "LDC-5/UHF" calibrator, injecting pulses from 5 pC up to 500 pC. Additionally, the noise test was performed with the same calibrator, injecting a constant 50 pC pulse in parallel with a BK wave generator, providing a 100 MHz bandwidth Gaussian noise of 100 mV to 1 V amplitude. Finally, using the BK wave generator, the frequency dependence test was performed by injecting pulses with a duration from 2.4 to 15 ns (the largest possible pulse width due to reflection in the GIS).

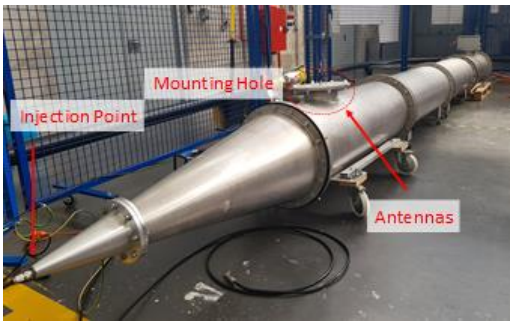

Fig. 2 LCOE LV setup.

2) *High-voltage test setup*

TUDelft, LCOE, and SGI participated using the following test setups.

Fig. 3 a) presents the HV test setup used by TUDelft, indicating the antennas' and reference's connections. The IEC 60270 method and a high-frequency current transformer (HFCT) were used as the reference measurement. On the one hand, the conventional method provides a measurement with a high signal-to-noise ratio but inaccuracy for high repetition discharges. On the other hand, the HFCT's current integration method ([15]) is more affected by noise but not by the repetition rate. Both reference methods are triggered simultaneously and compared in the oscilloscope.

The defects, generated with AC and DC+/- HV sources, consisted of 4 bar_{rel} SF_6-filled test cells with a protrusion, a surface defect (SD), a jumping particle (JP), and a 1 bar_{rel} floating electrode (FE). Due to the protrusion and surface defects low PD magnitudes, the ZFL-500LN+ amplifier was used for these defects. Additionally, the signals were filtered with 190 MHz low pass 8th order filters. The floating electrode has a low repetition rate for DC voltages. Therefore, the FE discharge was accelerated by pre-discharging it with a protrusion, similar to what was done in [16]. Fig. 3 b) shows a picture of the full-scale GIS, indicating the antennas, coupling capacitor, and test cells' position. The antenna position "A1" was 75 cm from the next spacer, and "A4" 90 cm to the T-section.

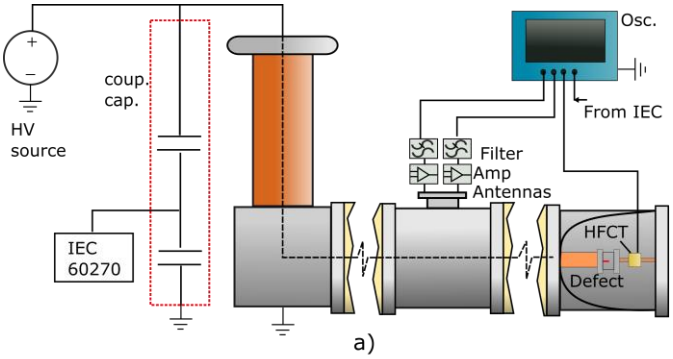

a)

b)

Fig. 3 a) TUDelft HV test setup and b) a picture of the full-scale GIS.

LCOE used the same GIS from Fig. 2 but with a HV configuration. Fig. 4 shows the antennas, the test cells, and the coupling capacitor, which was used as the reference. The SF_6 test cells were installed 1 m from the antennas. The pulses were generated in the test cells with an AC and a DC+/- source and were measured according to the IEC 60270 method. The signal coming from the measuring impedance and the antennas were recorded simultaneously with the oscilloscope. Due to the low amplitudes of protrusion and surface defects, both antennas were connected to the oscilloscope through Mini-Circuits ZFL-500LN+ amplifiers.

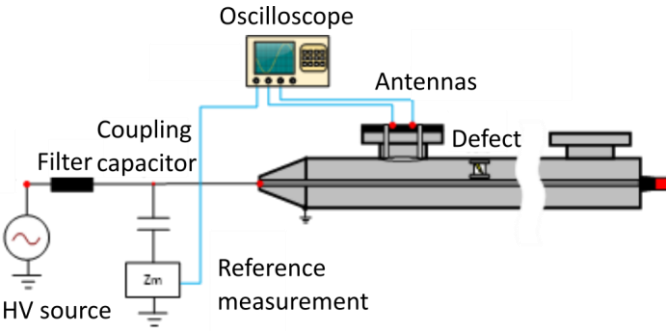

Fig. 4 Schematic of the LCOE HV test setup.

SuperGrid Institute used the GIS presented in Fig. 5. This HV test setup used a DC negative power supply connected with a full-size GIS through a coaxial HV cable. The setup comprised an HV protecting resistor, a coupling capacitor for conventional measurements, and a test compartment filled with 5.5 bar_{rel} SF_6. In this compartment, the defects (either a protrusion or a jumping particle held by a wire) and the sensors were placed, including a measurement electrode connecting the defect to ground through the reference sensor. Depending on the test, several sensing systems were acquired in parallel with an oscilloscope, among:

- Conventional apparent charge according to IEC 60270.
- Magnetic sensor with amplifier Femto HCA-400M-5K-C.
- UHF sensor with amplifier R&K LA-120-0S.
- HFCT or current probe on the measurement electrode.

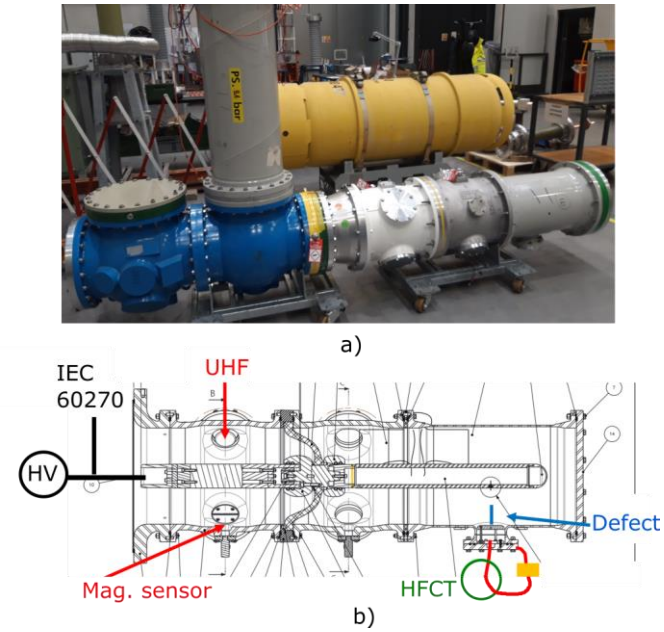

Fig. 5 a) Picture of the test setup and b) schematic of the sensor placed in it.

The noise was applied with a function generator placed between the end of the enclosure and the earth of the test platform, so the noise propagated in the enclosure. Two different noises were used: a 10 V sinewave at 20 MHz and a white noise with components up to 20 MHz with an applied amplitude of up to 10 V.

B. Sensor's characterization and calibration

1) Sensors design for each calibration setup

Each participant laboratory has a unique GIS geometry, resulting in a different magnetic and electric sensor design. Although the sensors differ in dimensions, all sensors' principles are the same. For TUDelft and LCOE, the electric antenna was a handmade disk-type UHF sensor sharing the same mounting hole with the magnetic sensor. On the other hand, SGI used a commercial disk-type UHF installed in a dedicated mounting hole located in the same transversal position as the magnetic sensor. Having the antennas in the same transversal position ensures the PD pulse electromagnetic field simultaneous arrival for both antennas. A balanced magnetic loop antenna design was chosen for all laboratories, giving higher common mode noise rejection [17]. Fig. 6 to Fig. 8 show each laboratories sensors and their dimensions. TUDelft used different setups for the HV and LV tests, giving different antennas' electric parameters.

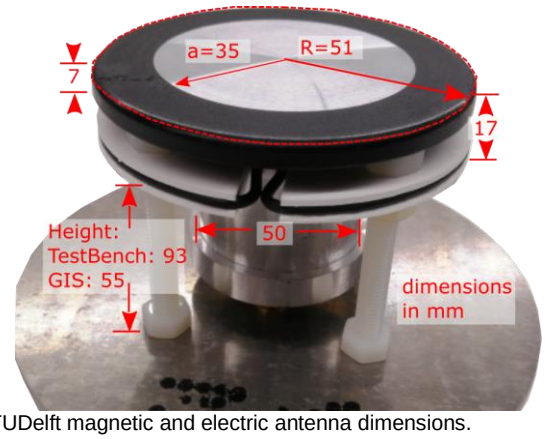

Fig. 6 TUDelft magnetic and electric antenna dimensions.

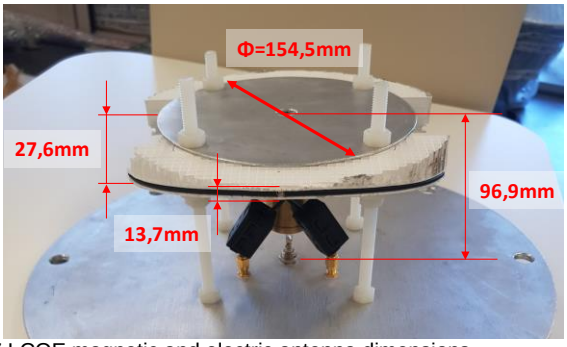

Fig. 7 LCOE magnetic and electric antenna dimensions.

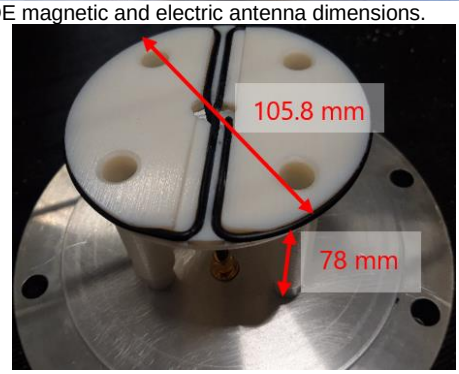

Fig. 8 SGI magnetic antenna dimensions.

2) *Sensors' parameters and calibration constants*

Following the frequency-domain calibration procedure in [6], the calibration constants for each laboratory were obtained. Taking LCOE calibration as an example, the frequency-domain method and a proposed time-domain method are compared and explained in this section.

For the frequency-domain calibration, LCOE injected 15 V_{pp} sinusoidal signals with frequencies between 10 kHz and 120 MHz in the test setup shown in Fig. 2. The magnetic sensor was characterized by measuring its output voltage and the injected current through an HFCT. For the electric antenna, the voltage at the injection point and the antenna's output were measured directly on the oscilloscope. In order to reduce the noise, an average of 5 measurements were performed. Fig. 9 shows the measured frequency responses (H) and the linear fit, whose slope represents the a) magnetic and b) electric antennas calibration constants (k_m =1.50 nΩs, and k_e=3.16 nΩs). The frequency responses show resonances starting around 10 MHz, generated by the GIS unmatched length. Therefore, the sensor's sensitivity limits the lowest frequency to be considered, whereas the GIS resonance limits the highest frequency in the calibration constant calculation. In this case, the calibration constants (k_e and k_m) were found in the frequency range between 10-500 kHz.

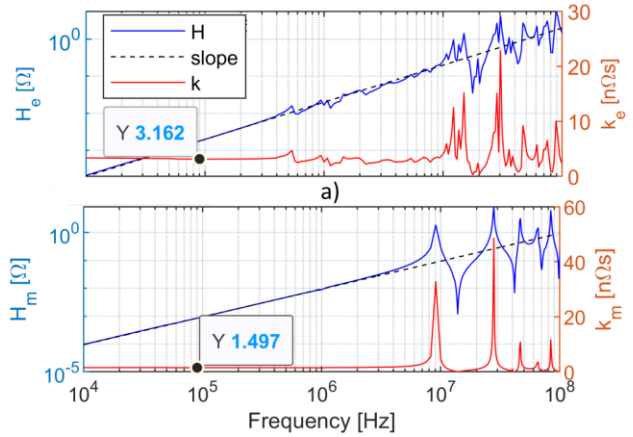

Fig. 9 LCOE frequency-domain calibration for the a) electric and b) magnetic sensors, where *k* corresponds to the calibration constants.

To validate the antennas' calibration constants, LCOE proposed a time-domain method where a linearity test was performed using a calibrator. One hundred PD pulses were injected for each charge between 5 pC and 500 pC, where the injected PD pulse and the antennas' output signals were measured simultaneously. The injected PD pulse was measured with a reference HFCT. The injected PD pulse charge (Q_{HFCT}) was calculated by direct integration of the measured PD pulse current [15], whereas for the antennas, the voltage-double-integral method was applied without considering any calibration constant (Q'_m for the magnetic antenna and Q'_e for the electric one). Considering that in the V2I method, the charge is inversely proportional to the calibration constant (3), these were calculated by dividing the antenna's estimated charge by the charge measured with the HFTC ($k_m'=Q'_m/Q_{HFCT}$ and $k'_e=Q'_e/Q_{HFCT}$). As shown in Table 1, the calibration constants resulting from the time-domain approach (k'_m=1.49 nH and k'_e =3.20 nΩs) were very close to the calculated ones from the frequency response, which confirms the obtained values.

Table 1. Verification of the calibration constants of the antennas employing a linearity test

Q_{inj} [pC]	Q'_m [pC]	Q'_e [pC]	k'_m [nΩ·s]	k'_e [nΩ·s]
25	3.62E-08	8.00E-08	1.45	3.20
50	7.45E-08	1.60E-07	1.50	3.22
100	1.49E-07	3.22E-07	1.50	3.22
200	2.97E-07	6.39E-07	1.49	3.21
350	5.24E-07	1.13E-06	1.49	3.22
500	7.50E-07	1.61E-06	1.50	3.22
		Mean	1.49	3.20
		std (%)	0.29%	0.76%

The rest of the antenna's electrical parameters are used in the synergy method and were found in different ways by each laboratory. LCOE used an RLC bridge to measure the magnetic sensor's self-inductance (L_s) and the electric sensor's parasitic capacitance (C_2). TUDelft found the values by fitting the model (1) with the frequency response measured in the test bench. Also, TUDelft and SGI calculated the parameters using a finite element method simulation. These parameters are presented in Table 2.

Table 2 Electric and magnetic sensors' parameters for each laboratory.

Antenna parameters	TUDelft – LV/HV	LCOE	SGI
k_m [nΩs]	0.56/0.68	1.50	1.1
L_s [nH]	161	290	186
k_e [nΩs]	0.73/2.05	3.24	1.2
C_2 [pF]	33/35	14.3	6.5
R [Ω]	50	50	50
Z_0 [Ω]	50/65	50	85

III. Results and Discussion

This section presents the calibration method's uncertainty in the different laboratories' LV and HV test setups.

A. LV test results

1) *TUDelft*

Fig. 10 to Fig. 12 show the average and standard deviation error of 100 samples for each test. Fig. 10 shows the uncertainty for different charge values. As expected, the average does not change with the PD magnitude; however, at high charge values, the mean error rises due to the amplifier's dynamic range. The amplifier saturates with high-magnitude PD. Conversely, the standard deviation decreases with the charge magnitude, attributed to the higher signal-to-noise ratio (SNR). Fig. 11 shows the uncertainty for different pulse widths. In the case of the magnetic antenna, the average error is maintained almost constant for longer pulses, which is not the case for the electric antenna. This is attributed to the pulses bandwidth and the carbon-black-epoxy non-frequency linearity. Due to the SNR decrease, the standard deviation increases with the pulse width. In conclusion, the magnitude linearity and pulse widths are mainly affected by the noise.

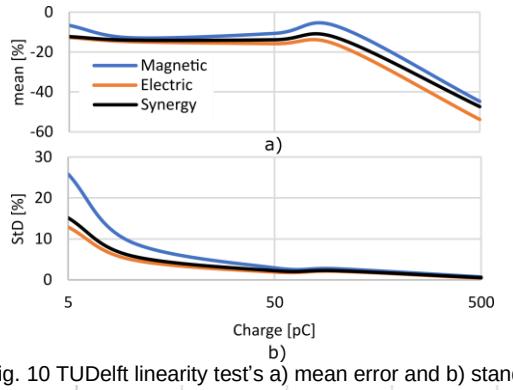

Fig. 10 TUDelft linearity test's a) mean error and b) standard deviation.

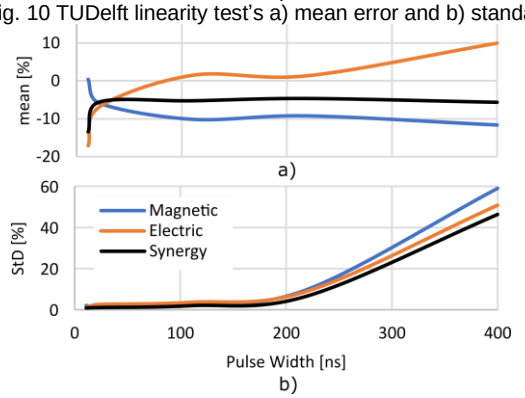

Fig. 11 TUDelft pulse width test's a) mean error and b) standard deviation.

Fig. 12 shows the uncertainty for different noise levels, represented as the RMS-noise-to-signal-peak ratio (NPR). The white noise is a random error, and it is expected that the mean error is not affected in a large batch, which was not observed in the results. A random noise has the same probability of increasing or decreasing the signal integration time. However, the output charge depends quadratically on the integration time, over-estimating the charge. The standard deviation increases with noise showing the same trend as the other tests.

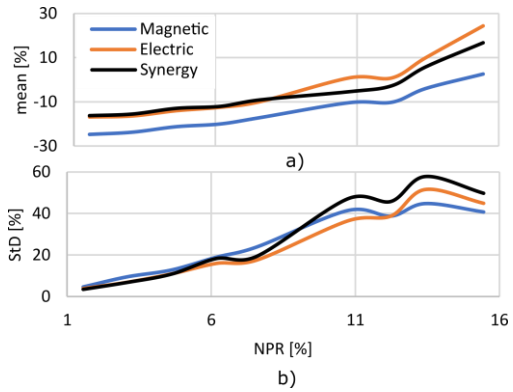

Fig. 12 TUDelft noise level test's a) mean error and b) standard deviation.

2) *LCOE*

For the linearity test, 100 reference pulses were injected into the GIS using the calibrator. Fig. 13 shows the mean and standard deviation errors between the injected PD charge and the sensors. Due to the magnetic antenna's lower sensitivity and the non-use of amplifiers, the mean error at low charges (≤10 pC) was significant; nevertheless, for higher charges, the mean error was below 0.5 %. For the electric antenna, due to its higher sensitivity, the mean error remained almost constant for all injected PD charges, between 1% and 3.6%. The standard deviation decreases as the PD charge increases due to the higher signal-to-noise ratio.

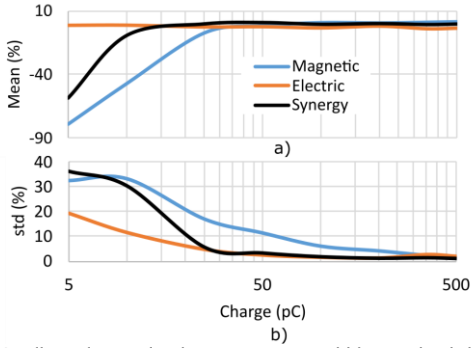

Fig. 13 LCOE linearity test's a) mean error and b) standard deviation.

The pulse width influence was determined by injecting 100 pulses with different durations. Fig. 14 shows the mean errors and standard deviation for the magnetic and electric antennas and the synergy method. Due to the reflection's limitation in the GIS, pulses with a duration higher than 14 ns could not be injected. The longer time of the pulses reduces the SNR of all antennas, especially the magnetic antenna, which has a lower sensitivity than the electric one. In the TUDelft tests, amplifiers were used to increase the sensitivity, and the gain difference between sensors was lower (see Table 2).

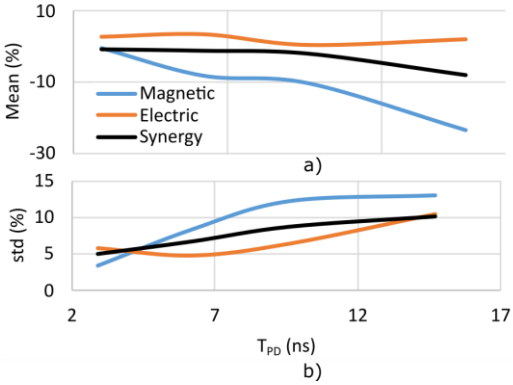

Fig. 14 LCOE pulse width test's a) mean error and b) standard deviation.

For the noise influence, superimposed Gaussian noise was injected between the GIS enclosure and the ground. One hundred PD pulses of 50 pC were injected and measured for each noise level. Fig. 15 shows the obtained mean errors and standard deviation for different noises. The measurement of the electric antenna was more affected by the noise, showing an increasing error with the noise level, whereas the magnetic antenna's absolute errors remained below 5%. The same behavior occurred for the standard deviation.

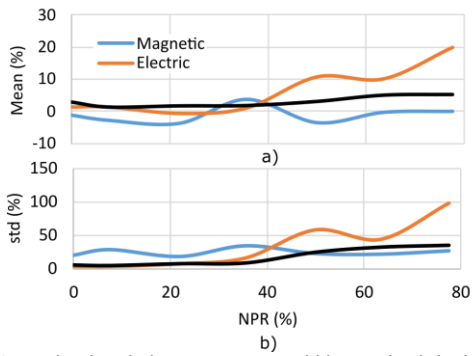

Fig. 15 LCOE noise level a) mean error and b) standard deviation.

The main uncertainty source for both laboratories is noise, affecting the magnitude and frequency linearity. Also, the V2I method loses accuracy when the pulse is not integrated to infinite. In the LV test, where there are no discontinuities, the synergy method gives an intermediate result from both antennas.

B. HV test results

The LV tests showed that the PD charge estimation error is mainly attributed to the noise and the V2I integration time. In the HV test, the full-scale GIS introduces more error sources, such as wave reflections, resonances, and calibration constant estimation, which are determined by the GIS size [6]. In the following subsections, the results for the three laboratories are tabulated, representing the magnetic antenna, the electric antenna, and the synergy as MA, EA, and Syn, respectively.

1) *TUDelft*

The mean and standard deviation errors are presented in Table 3. All PD defects' cutoff frequencies are above the sensor's bandwidth, meaning that the pulse widths do not affect the measurements. On the other hand, the PD defects magnitude affects the SNR and hence the charge estimation. The IEC method shows a high error for the protrusion and the DC floating electrode. This error is attributed to the corona high repetition and IEC low time resolution, resulting in overlapped pulses. This IEC low-resolution error is known from literature [18] and can be seen in Fig. 16, where three pulses are generated in less than 4 µs, resulting in an IEC overlapped measurement.

Overall, the antennas show an average error of around 30% for the high magnitude PD and about 1 pC difference in the low charge PD defects. The corona and SD low magnitude increase the measurement error; however, the IEC ±1 pC requirement keeps the measurement inside the tolerance. When the two antennas are combined, the measured reflections decrease, and the uncertainty improves, especially in the A4 location, where the antennas are more affected by the T-section discontinuity.

Table 3 Uncertainty results for TUDelft full-scale GIS.

			IEC/HFCT		MA/HFCT		EA/HFCT		Syn/HFCT	
			µ [%]	σ [%]	µ [%]	σ [%]	µ [%]	σ [%]	µ [%]	σ [%]
Jumping Particle	AC	A4	13	2	-42	3	-19	3	-27	2
		A1	12	6	-35	8	-45	3	-34	5
	DC+	A4	2	3	-25	2	-14	3	-12	2
		A1	4	3	-18	2	-25	2	-13	2
FE	DC-	A4	3	3	-30	2	-12	2	-13	2
		A1	0	3	-16	2	-24	2	-10	2
	AC	A4	29	8	-25	4	-9	4	-8	4
		A1	20	27	-22	5	-24	5	-20	5
	DC-	A4	328	356	-46	23	-36	27	-35	28
		A1	240	336	-32	20	-39	18	-29	20
Corona	AC	A4	72	39	-14	55	-6	15	-19	31
		A1	86	49	-27	24	-38	13	-27	18
	DC+	A4	144	64	-16	52	-17	16	-21	29
		A1	164	83	9	86	-42	17	-32	37
	DC-	A4	81	61	9	94	-17	21	-29	28
		A1	71	36	-24	31	-34	12	-28	19
SD	AC	A4	-2	33	-34	22	-29	13	-31	14
		A1	-11	27	-43	15	-38	11	-37	13

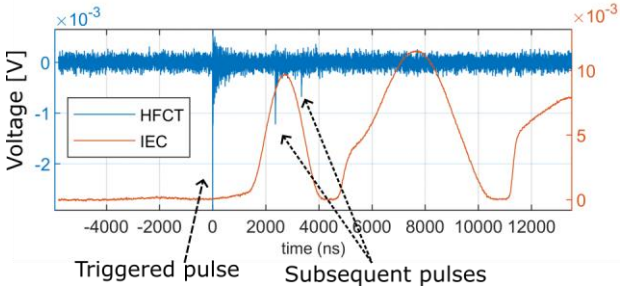

Fig. 16 Corona discharge waveshapes for the HFCT and the IEC method.

2) *LCOE*

Table 4 shows the HV test (AC and DC sources) results performed in the LCOE high-voltage setup, where 200 pulses of each defect were recorded and analyzed. Both antennas show an error below 30%, except for the protrusion defect, where the electric antenna's error was higher than the other defects. This is associated with the nonlinearity of the amplifiers when the charge is too low and the sensor's high input capacitance. In general, the antenna errors were lower when the synergy method was applied.

Table 4 Uncertainty results for LCOE full-scale GIS.

		MA/IEC		EA/IEC		Syn/IEC	
		µ (%)	σ (%)	µ (%)	σ (%)	µ (%)	σ (%)
SD	AC	-32	9	-10	10	6	12
FE	AC	-15	5	20	6	-1	5
	DC+	18	5	23	4	-5	4
	DC-	15	8	15	5	-8	5
JP	AC	-28	22	-12	38	-7	31
	DC+	-15	21	2	25	-25	33
	DC-	-18	26	5	27	14	47
Cor.	AC	-19	17	-76	8	-19	16

3) *SGI*

The tests performed at SuperGrid Institute gave the results presented in Table 5. First, tests were performed with a protrusion under DC- and without noise. Second, the JP tests were performed under DC- without and with two different noises, where N1 is the sinewave noise, and N2 is the white noise. Four thousand pulses were recorded for each configuration to have several amplitudes of discharges and for statistical analysis. The reference signal to evaluate the calibration was the HFCT or the conventional IEC system. Similar results to the other laboratories were obtained.

Table 5 Uncertainty results for SGI full-scale GIS.

				MA		EA	
		Ref.	Noise	μ (%)	σ (%)	μ (%)	σ (%)
Cor.	DC-	HFCT	No Noise	-20	23	-8	19
JP	DC-	IEC	No Noise	6	69	-7	31
JP	DC-	IEC	N1	17	23	-10	28
JP	DC-	IEC	N2	18	23	-1	27

IV. Conclusion

The GIS maintenance and installation high costs demand reliable online electric insulation monitoring. Present PD measuring systems sense the PD without measuring a calibrated charge that can assess the defect severity. Our study demonstrated a measuring system capable of estimating the PD charge in GIS with a reasonable error. The method's uncertainty evaluated in the low-voltage test bench gave slightly different values in the linearity, SNR, and pulse width test, with a mean error of around 10%. The proposed method was also tested in three full-scale GIS, having an average error of about 30%. These errors are above IEC PD tolerances. However, currently, no other online method can estimate PD charges in GIS. The main uncertainty of the proposed system originates from the background noise. Therefore, noise reduction technics must be investigated in order to improve the system's performance. With further investigation, this system is expected to compare online measurements with IEC 60270 laboratory tests. We believe these results pave the way for better GIS' insulation diagnosis.

References

[1] INTERNATIONAL, ELECTROTECHNICAL, and COMMISSION, *IEC 62271: High-voltage switchgear and controlgear – Part 203: AC gas-insulated metal-enclosed switchgear for rated voltages above 52 kV*, vol. 3. 2022.

[2] IEC 60270, "Partial Discharge Measurements," 2015.

[3] INTERNATIONAL, ELECTROTECHNICAL, and COMMISSION, *IEC 62478: High voltage test techniques – Measurement of partial discharges by electromagnetic and acoustic methods*, 1.0. International Standard, 2016.

[4] L. Hao *et al.*, "Discrimination of multiple PD sources using wavelet decomposition and principal component analysis," *IEEE Trans. Dielectr. Electr. Insul.*, vol. 18, no. 5, pp. 1702–1711, 2011, doi: 10.1109/TDEI.2011.6032842.

[5] A. Cavallini, G. C. Montanari, and M. Tozzi, "PD apparent charge estimation and calibration: A critical review," *IEEE Trans. Dielectr. Electr. Insul.*, vol. 17, no. 1, pp. 198–205, 2010, doi: 10.1109/TDEI.2010.5412018.

[6] C. Mier, A. Rodrigo Mor, L. Castro, and P. Vaessen, "Magnetic and electric antennas calibration for partial discharge charge estimation in gas-insulated substations," *Int. J. Electr. Power Energy Syst.*, vol. 141, no. January, p. 108226, 2022, doi: 10.1016/j.ijepes.2022.108226.

[7] A. Rodrigo-Mor, F. A. Muñoz, and L. C. Castro-Heredia, "Principles of charge estimation methods using high-frequency current transformer sensors in partial discharge measurements," *Sensors (Switzerland)*, vol. 20, no. 9, 2020, doi: 10.3390/s20092520.

[8] C. Mier, A. Rodrigo Mor, P. Vaessen, and A. Lathouwers, "Magnetic and electric antennas synergy for partial discharge measurements in gas-insulated substations: Power flow and reflection suppression," *Int. J. Electr. Power Energy Syst.*, vol. 144, no. January 2023, pp. 1–9, 2023, doi: 10.1016/j.ijepes.2022.108530.

[9] JCGM 2008:100, "Evaluation of measurement data — Guide to the expression of uncertainty in measurement," *International Organization for Standardization Geneva ISBN*, no. September. p. 134, 2008.

[10] A. Ferrero and S. Salicone, "Measurement uncertainty," *IEEE Instrum. Meas. Mag.*, vol. 9, no. 3, pp. 44–51, 2006, doi: 10.1109/MIM.2006.1637979.

[11] M. Hikita, S. Ohtsuka, T. Teshima, S. Okabe, and S. Kaneko, "Electromagnetic (EM) wave characteristics in GIS and measuring the em wave leakage at the spacer aperture for partial discharge diagnosis," *IEEE Trans. Dielectr. Electr. Insul.*, vol. 14, no. 2, pp. 453–460, 2007, doi: 10.1109/TDEI.2007.344624.

[12] W. Boeck, W. Buesch, E. Colombo et al., "Insulation Co-ordination of GIS: return of experience, on site tests and diagnostic techniques," Electra No.176, JWG 33/23.12, February 1998.

[13] A. J. Reid, M. D. Judd, B. G. Stewart, and R. A. Fouracre, "Partial discharge current pulses in SF6 and the effect of superposition of their radiometric measurement," *J. Phys. D. Appl. Phys.*, vol. 39, no. 19, pp. 4167–4177, 2006, doi: 10.1088/0022-3727/39/19/008.

[14] H. Okubo, N. Hayakawa, and A. Matsushita, "The relationship between partial discharge current pulse waveforms and physical mechanisms," *IEEE Electr. Insul. Mag.*, vol. 18, no. 3, pp. 38–45, 2002, doi: 10.1109/MEI.2002.1014966.

[15] A. R. Mor, P. H. F. Morshuis, and J. J. Smit, "Comparison of charge estimation methods in partial discharge cable measurements," *IEEE Trans. Dielectr. Electr. Insul.*, vol. 22, no. 2, pp. 657–664, 2015, doi: 10.1109/TDEI.2015.7076760.

[16] S. Abdul Madhar, P. Mraz, A. Rodrigo Mor, and R. Ross, "Physical interpretation of the floating electrode defect patterns under AC and DC stress conditions," *Int. J. Electr. Power Energy Syst.*, vol. 118, no. July 2019, p. 105733, 2020, doi: 10.1016/j.ijepes.2019.105733.

[17] C. M. Escurra and A. R. Mor, "Balanced Magnetic Antenna for Partial Discharge Measurements in Gas-Insulated Substations," in *2022 9th International Conference on Condition Monitoring and Diagnosis, CMD 2022*, 2022, pp. 509–512, doi: 10.23919/CMD54214.2022.9991698.

[18] A. Pirker and U. Schichler, "Partial discharge measurement at DC voltage -Evaluation and characterization by NoDi∗ pattern," *IEEE Trans. Dielectr. Electr. Insul.*, vol. 25, no. 3, pp. 883–891, 2018, doi: 10.1109/TDEI.2018.006742.